

New ACV variables discovered in the Zwicky Transient Facility survey

B. Bauer-Fasching¹, K. Bernhard^{2,3}, E. Brändli¹, H. Burger¹, B. Eisele¹, S. Hümmerich^{2,3}, J. Neuhold¹, E. Paunzen⁴, M. Piecka¹, S. Ratzenböck^{1,5}, and M. Prišegen⁶

¹ Department of Astrophysics, Vienna University, Türkenschanzstraße 17, 1180 Vienna, Austria

² Bundesdeutsche Arbeitsgemeinschaft für Veränderliche Sterne e.V. (BAV), Berlin, Germany

³ American Association of Variable Star Observers (AAVSO), Cambridge, USA

⁴ Department of Theoretical Physics and Astrophysics, Faculty of Science, Masaryk University, Kotlářská 2, 611 37 Brno, Czechia

⁵ University of Vienna, Research Network Data Science at Uni Vienna, Kolingasse 14-16, 1090 Vienna, Austria

⁶ Advanced Technologies Research Institute, Faculty of Materials Science and Technology in Trnava, Slovak University of Technology in Bratislava, Bottova 25, 917 24 Trnava, Slovakia

ABSTRACT

Context. The manifestation of surface spots on magnetic chemically peculiar (mCP) stars is most commonly explained by the atomic diffusion theory, which requires a calm stellar atmosphere and only moderate rotation. While very successful and well described, this theory still needs to be revised and fine-tuned to the observations.

Aims. Our study aims to enlarge the sample of known photometrically variable mCP stars (ACV variables) to pave the way for more robust and significant statistical studies. We derive accurate physical parameters for these objects and discuss our results in the framework of the atomic diffusion theory.

Methods. We studied 1314 candidate ACV variables that were selected from the Zwicky Transient Factory catalogue of periodic variables based on light curve characteristics. We investigated these objects using photometric criteria, a colour-magnitude diagram, and spectroscopic data from the LAMOST and *Gaia* missions to confirm their status as ACV variables.

Results. We present a sample of 1232 new ACV variables, including information on distance from the Sun, mass, fractional age on the main sequence, fraction of the radius between the zero-age and terminal-age main sequence, and the equatorial velocity and its ratio to the critical velocity.

Conclusions. Our results confirm that the employed selection process is highly efficient for detecting ACV variables. We have identified 38 stars with v_{equ} in excess of 150 km s^{-1} (with extreme values up to 260 km s^{-1}). This challenges current theories that cannot explain the occurrence of such fast-rotating mCP stars.

Key words. stars: chemically peculiar – stars: variables: general – stars: rotation

1. Introduction

The classical chemically peculiar (CP) stars of the upper main sequence have been targets of detailed investigations since their first detection by Maury & Pickering (1897). They are excellent test objects for astrophysical processes such as diffusion, convection, and stratification in stellar atmospheres. There is a wide variety of peculiar stars in the spectral domain from B0 (30000 K) to F5 (6500 K). Preston (1974) divided the CP stars into four groups based on the presence of strong magnetic fields and the kind of surface elemental peculiarity.

The magnetic chemically peculiar (mCP) stars, which encompass the Ap/CP2 stars and He-peculiar stars groups (Preston 1974), exhibit peculiar surface abundances and a non-uniform distribution of certain chemical elements. They also possess strong and global magnetic fields. The CP2 stars show overabundances of Si, Sr, Cr, Eu, and the rare-earth elements as compared to the solar composition (e.g. Preston 1974; Saffe et al. 2005; Gray & Corbally 2009; Ghazaryan et al. 2018). The He-peculiar stars comprise the B5 to B9 He-weak (CP4) stars that show anomalously weak He I lines for their temperature type, and the more massive B1 to B3 He-strong stars with anomalously strong He I lines (Andrillat & Jaschek 1998; Ghazaryan

et al. 2019). Other groups of CP stars include the metallic-line (Am/CP1) stars and the mercury-manganese (HgMn/CP3) stars; they, however, are only marginally relevant to the present study and will not be discussed here in detail.

Many mCP stars exhibit strictly periodic changes in their spectra and brightness in different photometric passbands, which result from a flux redistribution in the unevenly distributed surface abundance patches (‘chemical spots’) of certain elements (Krtička et al. 2012) and are satisfactorily described by the oblique rotator model (Stibbs 1950). Amplitudes of several hundredths up to some tenths of a magnitude are observed (Netopil et al. 2017), and the amplitude of the light variability generally increases towards shorter wavelengths. These photometrically variable mCP stars are traditionally called α^2 Canum Venaticorum (ACV) variables. Depending on the distribution of surface spots and the magnetic field characteristics, ACV variables show an amazing diversity of light curves (Jagelka et al. 2019). The latest version of the International Variable Star Index (VSX; Watson et al. 2006) lists 1768 known ACV variables.

For the manifestation of surface spots of different elements, a calm stellar atmosphere and only moderate rotation are required (Michaud et al. 1981). Otherwise, the observed surface patterns become unstable and are destroyed. However, while the general

framework of this complex mechanism has been well described, it still needs to be revised and adapted to observations.

The present study aims to enlarge the sample of known ACV variables using data from the *Zwicky* Transient Facility (ZTF) survey in order to pave the way for more robust and significant statistical studies. It follows up and concludes the feasibility study of Faltová et al. (2021), who identified 1400 candidate ACV variables via photometric criteria and published the 86 most promising candidates.

We present an investigation of the remaining 1314 candidates, taking into account, whenever available, spectroscopic data from the Large Sky Area Multi-Object Fiber Spectroscopic Telescope (LAMOST) and *Gaia* missions to confirm their status as CP objects. We assembled a final sample of 1232 ACV variables, for which we derive astrophysical parameters and rotational velocities. We conclude by discussing our results in the framework of models that explain the CP star phenomenon.

Data sources are summarised in Section 2. General methods and results are described in Section 3; a search for membership in open star clusters is detailed in Section 4. Finally, we discuss our results and conclude in Section 6.

2. Data sources

This section briefly summarises the employed data sources.

2.1. The *Zwicky* Transient Facility survey

In this study, we relied on data from the ZTF, a public-private partnership optical time-domain survey that uses the 48-inch Samuel Oschin Schmidt telescope situated at the Palomar Observatory in northern San Diego County, California, which is optimised for spectral classification of stars brighter than 19 mag (Graham et al. 2019), in conjunction with a wide field CCD camera with a 47 deg² field of view (Bellm et al. 2019a). In addition, an integral field unit spectrograph is employed on the Palomar 60-inch telescope that is used to identify transients over a significant fraction of the available sky and for dedicated spectroscopic follow-up observations. The acquired data were subsequently prepared in the Infrared Processing and Analysis Center (IPAC). The ZTF survey provides nearly 300 epochs each year per object in the northern hemisphere and produces high-quality light curves in the *g*, *r*, and *i* bands.

Due to the large area covered by the survey, the ZTF is a powerful facility for identifying transits or acquiring time-series photometric observations (Graham et al. 2019). Its aims are the discovery of young supernovae and transits in general but also the study of active galactic nuclei, observation of asteroids and variable stars. For more information on the ZTF, we refer the reader to Bellm et al. (2019b) and Masci et al. (2019).

2.2. The Large Sky Area Multi-Object Fibre Spectroscopic Telescope (LAMOST)

Whenever available, spectra from the LAMOST survey were employed in the investigation of our sample stars. LAMOST is operated at Xinglong Station Observatory in China and managed by the National Astronomical Observatories from the Chinese Academy of Sciences (NAOC). It obtains spectra from the northern sky using a reflecting Schmidt telescope with primary mirror size of 4 metres and 4000 movable fibres to survey an equal number of objects simultaneously.

We used LAMOST low-resolution spectra, which have a spectral resolution $R \sim 1800$ and wavelength coverage from 3700 Å to 9000 Å. More information on the LAMOST project can be gleaned from Zhao et al. (2012) and Cui et al. (2012).

2.3. The *Gaia* mission BP/RP spectra

The *Gaia* mission (Gaia Collaboration et al. 2021) provides a wealth of low-resolution blue photometer and red photometer (BP/RP) spectra, which cover the wavelength region from 3300 Å to 10500 Å with a resolving power between 25 and 100, depending on the wavelength (Carrasco et al. 2021). Taking into account variations over the focal plane, all spectra are brought onto a common flux and pixel (pseudo-wavelength) scale. A mean spectrum is produced from multiple observations of the same source. *Gaia* Data Release (DR) 3 already includes about 219 000 000 mean BP/RP spectra for objects up to the 18th magnitude in *G*. The signal-to-noise ratio depends on the apparent magnitude and colour of the object. For more information on the *Gaia* BP/RP spectra, we refer the reader to Carrasco et al. (2021) and Montegriffo, P. et al. (2023).

3. Methods and results

This section describes the methods and, where appropriate, the corresponding results obtained in this study.

3.1. Target selection

The present paper is a follow-on work to the feasibility study of Faltová et al. (2021) and examines the 1314 candidate ACV variables that were identified but not further investigated by these authors. In the following, we provide a brief overview over the methodology employed by Faltová et al. (2021) to select these stars.

Based on ZTF DR2, Chen et al. (2020) compiled a catalogue of 781 602 periodic variable stars, which has been the principal source for target selection in Faltová et al. (2021). As ACV variables were not considered in the catalogue of Chen et al. (2020), it does not have a category for this kind of object, and it can be assumed (and has indeed been proved by Faltová et al. 2021) that ACV variables were consequently assigned to other categories, in particular to the class of the RS Canum Venaticorum (RS CVn) stars. These objects show rotational modulated light changes that, at least at first glance, resemble those of ACV variables. They are, however, close binary stars with active chromospheres and enhanced spot activity and thus a very different group of objects (e.g. Hall 1976), which can easily be distinguished from ACV variables by, for example, the use of a colour-magnitude diagram (CMD). The newest data of the *Gaia* mission now allow us to establish the CMD precisely and, therefore, to further select between ACV and RS CVn stars.

To identify ACV candidates among the 81 393 RS CVn stars listed in the Chen et al. (2020) catalogue, Faltová et al. (2021) applied several restrictions based on known characteristics of ACV variables (e.g. Netopil et al. 2017; Jagelka et al. 2019): (a) variability period between one and ten days; (b) amplitude in the *r* band of less than 0.3 mag; (c) the presence of a single independent variability frequency and corresponding harmonics; (d) stable or marginally changing light curve throughout the covered time span; and (e) an effective temperature between 6000 K and 25000 K (Andrae et al. 2018).

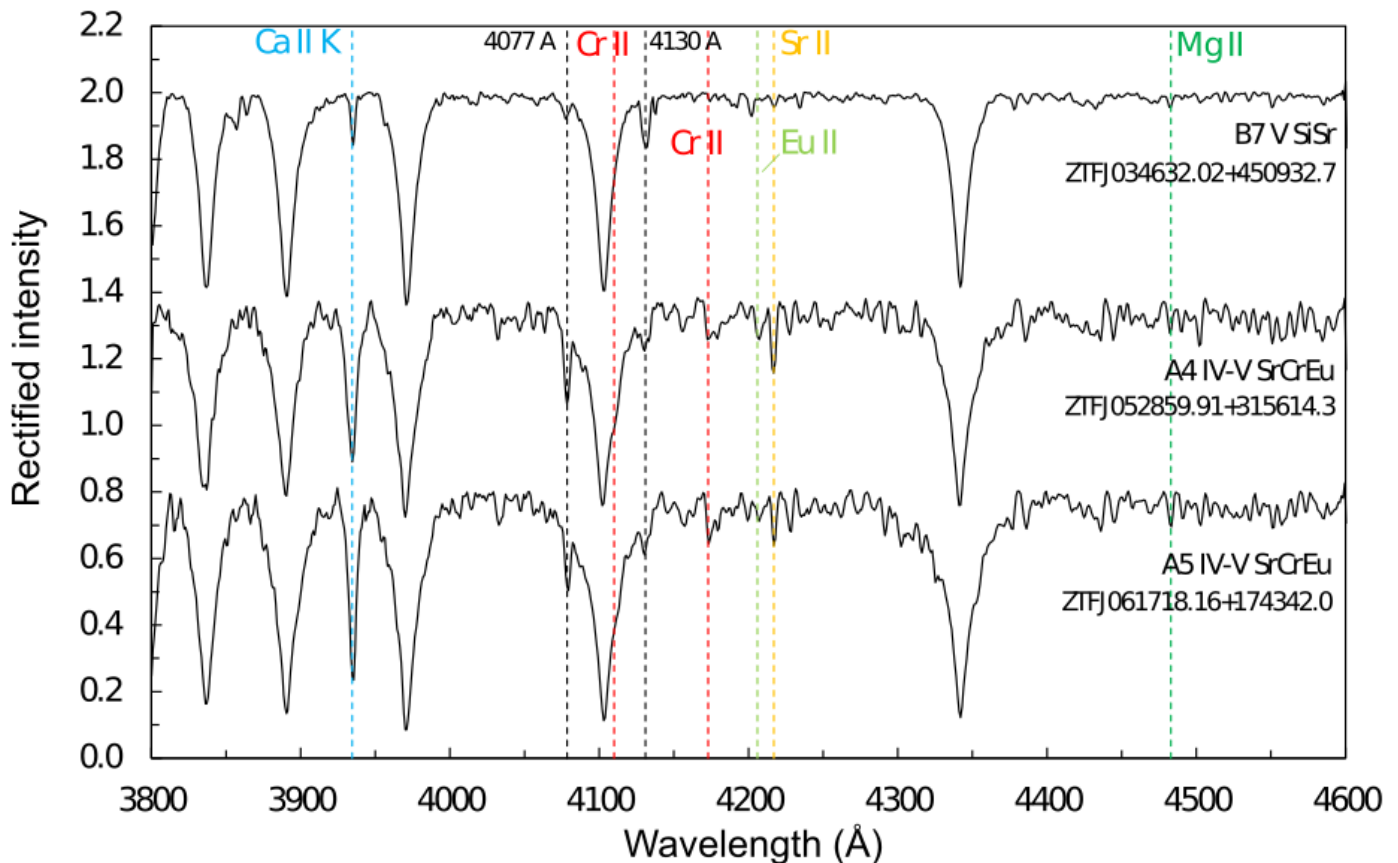


Fig. 1. Blue-violet region of the LAMOST spectra of (from top to bottom) the CP2 stars ZTFJ034632.02+450932.7 (B7 V SiSr), ZTFJ052859.91+315614.3 (A4 IV-V SrCrEu), and ZTFJ061718.16+174342.0 (A5 IV-V SrCrEu). Some prominent lines of interest are identified.

Item (c) was enforced to eliminate pulsating stars, which are mostly multi-periodic variables. Item (d) was chosen to distinguish ACV variables, whose light curves remain stable over very long periods of time (decades or more), from other spotted rotating variables, such as Sun-like stars or the aforementioned RS CVn variables, which are prone to exhibiting significant light changes as spots form and decay (e.g. Kozhevnikova & Alekseev 2015).

Out of the 81 393 stars identified as RS CVn stars by Chen et al. (2020), 1400 objects (1.7%) were identified through these criteria, whose ZTF light curves were then downloaded and visually inspected. The most promising 86 ACV candidates were then selected and published by Faltová et al. (2021), who identified several photometric peculiarities of these stars that can be employed in the identification of mCP stars: (1) the light curves in g and r are in anti-phase; (2) the amplitude of variability is larger in r than in g ; (3) the light curves show inconsistent shapes in g and r . Items (1) and (3) are, to the best of our knowledge, a peculiar characteristic of ACV variables and not seen in any other periodic variable stars. Item (2) is further proof that these stars are not pulsating variables, which are expected to show larger amplitudes at shorter wavelengths.

A total of 82 objects were eliminated from the sample because they did not meet these criteria. So, the final sample consists of 1232 stars. These objects were subsequently investigated in a CMD (cf. Sections 3.3 and 6); no RS CVn system, whose primary component is of spectral type F ($(BP-RP)_0 > +0.5$ mag) or later, was found in this way.

As a first step, the ZTF light curves of these 1232 stars were searched for periodicities using the packages *Period04* (Lenz & Breger 2005) and *Peranso* (Paunzen & Vanmunster 2016). Within the errors, we obtained the same results.

3.2. Classification

3.2.1. Spectral classification

We used low-resolution LAMOST spectra from DR7, which contains almost 10 million archival spectra.¹ Only spectra with $S/N > 20$ were considered. In summary, LAMOST spectra are available for 138 out of 1232 stars (11.2%) stars of our sample.

Spectral classifications were derived with the modified MKCLASS code² (`‘MKCLASS_mCP’`) of Hümmerich et al. (2020), which was specifically adapted to classify mCP stars, and the four libraries of standard star spectra used in the aforementioned study. For more information on the MKCLASS_mCP code, its usage, and the standard libraries, we refer the reader to Hümmerich et al. (2020).

All spectral types derived in this way were sanity-checked manually. We stress that this process did not include a detailed

¹ <http://www.lamost.org/dr7/v2.0/>

² MKCLASS is a computer program in C used to classify stellar spectra on the Morgan-Keenan-Kellman (MKK) spectral classification scheme (Gray & Corbally 2014). The installation guide and further information can be accessed under <https://www.appstate.edu/~grayro/mkclass/>

Table 1. 31 high-confidence ($P > 0.7$) star cluster members cross-matched with the catalogue by Hunt & Reffert (2023).

ZTF ID	G magnitude	Period	Host Cluster	A_V	e_{A_V}	E_{A_V}	$\log t$	$e_{\log t}$	$E_{\log t}$
J200951.70+353418.1	13.831	0.521112	Biurakan_2	1.24	1.17	1.31	6.85	6.84	6.90
J062002.59+015217.6	13.797	2.379216	CWNU_1313	1.13	0.98	1.23	8.85	8.28	8.88
J033223.16+522840.4	14.495	1.928368	Czernik_16	2.39	2.28	2.44	8.72	8.71	8.80
J201432.04+411038.0	14.267	1.118963	FSR_0219	2.82	2.63	2.96	6.80	6.78	6.90
J215149.43+512546.7	14.326	1.969323	FSR_0325	1.28	1.19	1.38	8.59	8.48	8.66
J011734.53+611800.9	14.513	7.143945	FSR_0534	2.24	2.08	2.40	7.82	7.70	8.09
J044516.35+412701.6	14.200	25.026750	FSR_0723	1.14	1.03	1.21	8.26	7.84	8.50
J064008.37+132722.9	16.121	3.117477	FSR_0975	1.13	0.97	1.35	8.70	8.41	8.77
J052351.16+340638.2	13.659	6.944821	Gulliver_53	1.24	1.15	1.34	8.18	8.11	8.49
J043443.42+471535.0	15.452	2.195395	HSC_1246	2.88	2.36	2.93	6.74	6.73	7.52
J063607.12+171242.5	14.879	1.246997	HSC_1552	2.15	2.04	2.37	8.42	7.85	8.70
J070208.33-015427.8	13.817	2.943846	HSC_1702	1.23	1.07	1.48	8.96	8.65	9.10
J195926.03+300327.9	15.549	4.431191	HSC_538	3.00	2.74	3.20	8.27	7.85	8.58
J201440.55+344546.3	15.393	1.032562	HSC_573	1.05	0.95	1.14	8.70	8.65	8.86
J003024.62+592954.5	13.492	1.140750	HSC_961	0.81	0.70	0.90	8.50	8.33	8.60
J003241.55+614801.4	13.945	16.965972	King_15	1.44	1.32	1.56	8.73	8.63	8.88
J225208.24+581943.3	14.214	3.349355	King_18	1.63	1.54	1.72	8.48	8.43	8.57
J052008.16+392257.0	14.190	1.638088	NGC_1857	1.90	1.65	1.95	7.59	7.48	7.76
J014526.32+603634.2	14.472	3.436379	NGC_659	1.54	1.52	1.57	7.30	7.23	7.32
J195237.02+292309.4	13.820	1.855895	NGC_6834	1.43	1.25	1.46	8.26	8.23	8.65
J021932.01+570718.5	13.644	0.739862	NGC_869	2.03	1.98	2.13	7.82	7.60	7.87
J012949.33+623838.8	13.495	1.133402	OC_0237	1.83	1.68	1.89	7.29	7.23	7.83
J061911.26+183722.3	12.951	1.975130	Skiff_J0619+18.5	0.74	0.63	0.84	8.41	8.12	8.60
J002959.84+624914.9	15.164	1.362381	Theia_1851	2.28	1.89	2.44	7.54	7.40	7.96
J003005.72+625033.5	15.123	1.324113	Theia_1851	2.28	1.89	2.44	7.54	7.40	7.96
J200119.65+333657.0	14.636	2.926105	Toepler_1	1.85	1.77	2.00	8.34	8.27	8.50
J042455.95+441934.8	14.144	0.696192	UBC_1263	2.18	1.97	2.36	7.51	7.41	7.59
J042906.37+442429.1	14.275	1.029576	UBC_1264	2.23	2.01	2.41	7.17	7.17	7.50
J220008.02+461842.6	13.864	2.545526	UBC_1600	1.66	1.55	1.77	8.30	8.10	8.49
J061925.50+152011.7	15.945	2.171823	UBC_438	1.58	1.47	1.64	8.69	8.64	8.71
J201257.42+355238.9	14.645	0.925454	UBC_580	0.48	0.39	0.56	8.84	8.70	8.87

manual classification on the system, although in rare instances, weak peculiarities that were not identified by the code were manually added to the classifications. In the few instances where the code only provided the non-MKK-standard ‘bl4077’ (strong blend at 4077 Å) and/or ‘bl4130’ (strong blend at 4130 Å) classifications (c.f. Hümmerich et al. 2020), these were resolved into the contributing elements by visual inspection of the spectra. We caution, however, that the here derived peculiarity type classifications are not exhaustive as weak or complicated peculiarities may have been missed in several objects.

Furthermore, mCP stars often show narrow and peculiar hydrogen-line profiles that are easily misinterpreted as belonging to stars of higher luminosity. This also impacts automatic classification routines such as the MKCLASS code and is probably the reason for the high luminosity classification of many of our sample stars, which should be regarded with caution. It is well established that mCP stars are generally main-sequence objects (e.g. Netopil et al. 2017).

According to our expectations, all 138 stars turned out to be classical CP2 stars. The individual classifications are listed in Table A.1. Some representative example spectra are shown in Figure 1.

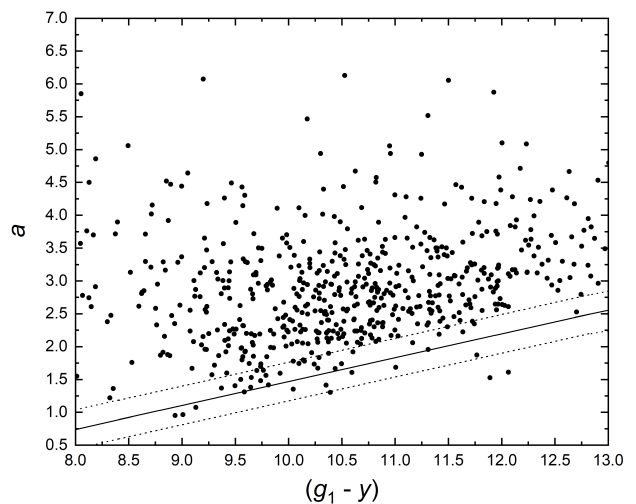


Fig. 2. Calculated synthetic Δa magnitudes (Paunzen & Prišegen 2022) for the 665 sample stars with *Gaia* BP/RP spectra. The dotted lines are the 95% prediction bands used to select mCP stars.

3.2.2. Probing the 5200 Å flux depression

Because LAMOST spectra are only available for a small fraction (11.2%) of our sample stars, we also had to resort to alterna-

tive means of establishing chemical peculiarities. We therefore checked for the presence of a flux depression at around 5200 Å, a spectral feature that is characteristic of mCP stars and caused by line blanketing of Cr, Fe, and Si enhanced by a magnetic field (Kupka et al. 2003; Khan & Shulyak 2007). While not all mCP stars show this flux depression, probably because they have an unfavourable inclination and the magnetic field characteristics (Paunzen et al. 2005), probing this spectral region has become a staple in the search for new peculiar stars (e.g. Maitzen & Seggewiss 1980a; Maitzen et al. 1998; Paunzen et al. 2005; Hümmerich et al. 2020; Shi et al. 2023).

As a first step, the available LAMOST spectra (cf. Section 3.2.1) were visually checked for the presence of the 5200 Å flux depression. According to our expectations, of the 138 stars with LAMOST spectra, 132 stars clearly show this feature.

Another approach to utilising the 5200 Å flux depression was presented by Paunzen & Prišegen (2022). These authors used *Gaia* BP/RP spectra (Carrasco et al. 2021) for the synthesis of Δa photometry, which refers to a photometric system specifically developed to measure the 5200 Å flux depression (e.g. Paunzen et al. 2005; Stigler et al. 2014). They synthesised Δa photometry for 1240 known mCP stars from BP/RP spectra and were able to effectively distinguish mCP stars from normal-type objects, with a detection level of more than 85% for almost the entire investigated spectral range (almost 95% for B- and A-type objects).

We followed the approach of Paunzen & Prišegen (2022) and calculated synthetic Δa magnitudes for the 665 sample stars with *Gaia* BP/RP spectra. In a nutshell, we normalised all spectra to the flux at 4020 Å and interpolated them in the wavelength region from 4800 Å to 5800 Å to a one-pixel resolution of 1 Å by applying a standard polynomial technique. Then the filter curves (with the central wavelengths as published by Maitzen & Seggewiss (1980b): g_1 5010 Å; g_2 5215 Å; y 5485 Å, and a bandwidth of 130 Å for each filter) were folded with the spectrum to calculate the synthetic magnitudes. Finally, all objects were investigated in the a versus $(g_1 - y)$ diagram. For more detailed information on this process, we refer the reader to the original paper (Paunzen & Prišegen 2022).

According to the 3σ level, 614 (92%) of this subsample of 665 stars was detected as mCP stars (Fig. 2). This is in accordance with the expectations from the abovementioned statistical studies about this group of stars.

3.3. Colour-magnitude diagram, age, and radius

The different *Gaia* data releases do not list astrophysical parameters for all of our target stars. Subsequently, the astrophysical properties of our sample stars were investigated in a CMD. To this end, we employed the homogeneous *Gaia* DR2 photometry from Arenou et al. (2018).³ For this photometric system, well-tested sets of PARSEC isochrones (Bressan et al. 2012) are available.

All our sample stars are situated farther than 500 pc from the Sun; therefore, interstellar reddening (absorption) cannot be neglected. To correct for this, we relied on the reddening map of Green et al. (2019) and the photogeometric distances from Bailer-Jones et al. (2021) to interpolate within this map. The transformation of the reddening values was performed using the relations

$$E(B - V) = 0.76E(BP - RP) = 0.40A_G. \quad (1)$$

³ We emphasise that the corresponding magnitudes from the more recent *Gaia* DR3 do not change the overall results in a significant way.

These relations already consider the conversion to extinction in different passbands using the coefficients listed in Green et al. (2018). The absolute magnitude for the *Gaia* G magnitude (M_G) of our target stars was calculated using the photogeometric distances and their errors from Bailer-Jones et al. (2021).

Ages, masses, and radii were estimated by the Stellar Isochrone Fitting Tool⁴ (Supikova & Paunzen 2021), which follows the methods described by Malkov et al. (2010). PARSEC isochrones (Bressan et al. 2012) for a solar metallicity of $Z = 0.017$ were used in this context, which has repeatedly been shown to be a good compromise for CP stars (e.g. Hümmerich et al. 2020; Paunzen et al. 2021).

To calculate the equatorial velocity (v_{equ}) assuming rigid body rotation, we used the relation from Preston (1971):

$$v_{\text{equ}} = 50.79R/P, \quad (2)$$

where R is the stellar radius in solar units, and P is the observed period in days. To determine $\sigma_{v_{\text{equ}}}$, we only have to consider the error of R because P is known with high precision. Recently, Eker & Bakış (2023) showed that R can be determined with an error less than 3% on a statistical basis. If we consider 5% and $2M_{\odot}$, we get $\sigma_{v_{\text{equ}}} = 5.1 \text{ km s}^{-1}$. Subsequently, we calculated the first critical velocity (v_{crit}) as adopted by Georgy et al. (2014) for the given metallicity (0.017) and individual stellar mass to obtain the velocity ratio $v_{\text{equ}}/v_{\text{crit}}$.

We extracted age and radius for a given mass at the terminal-age main sequence (TAMS), t_{TAMS} and r_{TAMS} , from the PARSEC isochrone grid. Finally, the ratio t/t_{TAMS} and r/r_{TAMS} was calculated.

4. Members of open clusters

The membership of a studied star in a coeval star group, such as an open cluster, can be used to put tighter constraints on the fundamental properties of the star, such as its distance, age, and initial metallicity, as all open cluster members share these properties to a high degree of approximation. In such stellar groupings, the ensemble of several tens to hundred open cluster members allows the determination of the properties of the studied star to significantly better precision and confidence, which would not be achievable if the star was studied in isolation. For this reason, identifying open cluster members among our studied sample of mCP stars might be of great value.

We used the star cluster membership lists from the catalogue of Hunt & Reffert (2023) to identify possible open cluster members among the studied stars. This catalogue contains the parameters of 7 167 star clusters, with more than 700 newly discovered high-confidence star clusters. In addition to this, the study also includes a list of cluster members with membership probabilities for each listed star. We cross-matched our final sample with these lists and identified 31 high-confidence ($P > 0.7$) star cluster members, which are presented in Table 1.

In a subsequent step, we determined the reddening values and ages of the host open clusters. In contrast to a single star, through which multiple isochrones can pass, coeval stellar systems can lift the degeneracy by populating a large magnitude range in the CMD. In the limit of error-free measurements in conjunction with perfectly tuned isochrone models, determining precise stellar parameters is a trivial task achieved by minimising the geometric distances between the data and model curves. However, observational data may be influenced by factors like

⁴ <https://github.com/Johaney-s/StIFT>

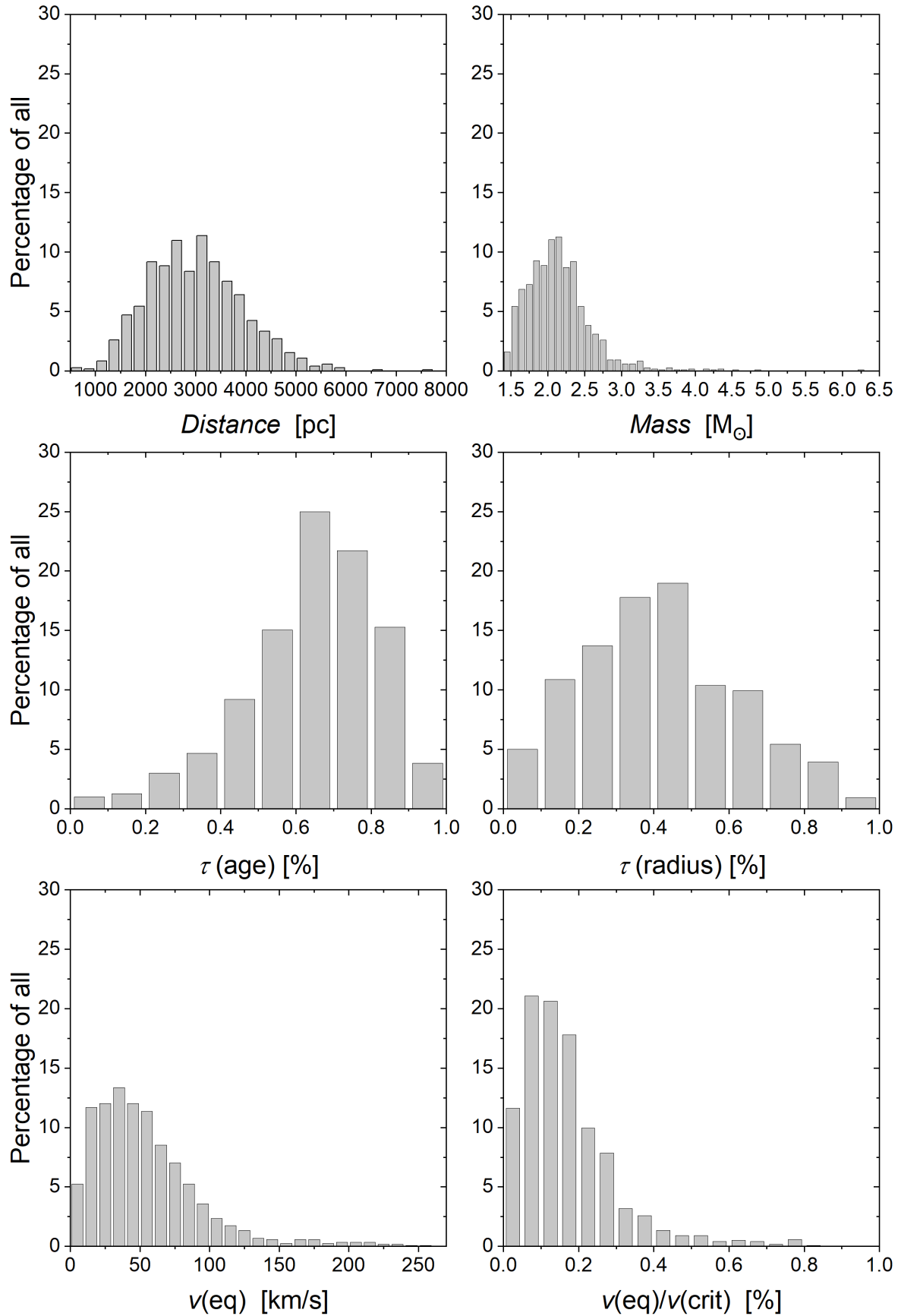


Fig. 3. Distributions of the distance from the Sun (upper-left panel), mass (upper-right panel), fraction of life spent on the main sequence (middle-left panel), fraction of radius between the ZAMS and TAMS (middle-right panel), equatorial velocity (lower-left panel), and ratio of equatorial to critical velocity (lower-right panel).

reddening, resolution limits, and contamination from the field. Other effects, such as intra-cluster metallicity variations or stellar rotation, can also cause deviations from model isochrones. Identifying the precise nature of each data point's deviation is often impossible, making it important to account for all these factors when choosing an appropriate statistical model.

We employed the isochrone fitting procedure from Ratzenböck et al. (2023), which models noise contributions around isochronal curves as samples drawn independently from skewed Cauchy distributions. The authors propose the skewed Cauchy distribution as it naturally incorporates non-symmetric noise sources, such as unresolved binaries and differential reddening effects inside the cluster. Additionally, the Cauchy distribution's heavy tails are known for their robustness to outliers and ability to model data with many outliers (Hampel et al. 2011), decreasing the correlation strength of derived parameters to imperfections in the sample selection. Assuming a constant noise model for every data point along the isochrone, we obtain parameter uncertainties by applying Bayes' theorem; the factorised Cauchy distribution becomes the likelihood while prior ranges are adopted from Ratzenböck et al. (2023).

We initialised Chronos by setting the metallicity to be constant (solar). Moreover, we used the distances from Hunt & Reffert (2023) and kept them fixed since they are expected to be already very precise. They list mean errors of below 5% for all their investigated clusters. Extinction and age are kept as free parameters. Unlike in the case of using the reddening map of Green et al. (2019), we find that for clusters and Chronos, the best choice for transforming A_V to extinction in *Gaia* bands is the following: $A_G = 0.857A_V$, $E(BP - RP) = 0.518A_V$. These values were derived by applying the Fitzpatrick & Massa (2007) extinction curves with $R_V = 3.1 - 3.3$ to the *Gaia* DR3 passbands. The chosen extinction coefficients almost coincide with the constant terms of the polynomials recommended for *Gaia* DR2 extinction, although they are somewhat shifted compared to the *Gaia* DR3 polynomials.

For the first guess of cluster parameters in Chronos, we used the age and extinction values from Hunt & Reffert (2023) to set the corresponding prior ranges to be within one order of magnitude in logarithmic age and within 1.5 mag around these values, respectively. The initial fit was then used to manually set the ranges (usually decreasing them), which were then used in the statistical fitting performed by Chronos. The lower and upper bounds of the extracted parameters are at 5 and 95 percentiles, respectively. All results are presented in Table 1.

It should be pointed out that some of the clusters show a complicated posterior distribution. This is caused either by having a small sample of stars that do not populate a main sequence or by having many outliers in the red giant regions. For this reason, Chronos was not able to find a narrow range of cluster parameters for the following objects: CWN 1313, FSR 0975, HSC 538, HSC 1552, King 15, NGC 1857, and UBC 1264. Moreover, the procedure did not correctly fit the parts of the main sequences of NGC 659 and UBC 1264, which are least affected by differential reddening. Finally, we note that the data distribution in the CMD of UBC 1264 shows an uncharacteristically prominent knee (at $BP - RP = 0.5$ mag) for a cluster of the fitted age. However, the isochrone corresponding to the lower bounds of age and extinction fit the data very well.

We have identified three stars that are members of star clusters younger than 10 Myr. According to their locations in the CMD, these objects just reached the zero-age main sequence (ZAMS). Then, there is a continuous sequence until the age of

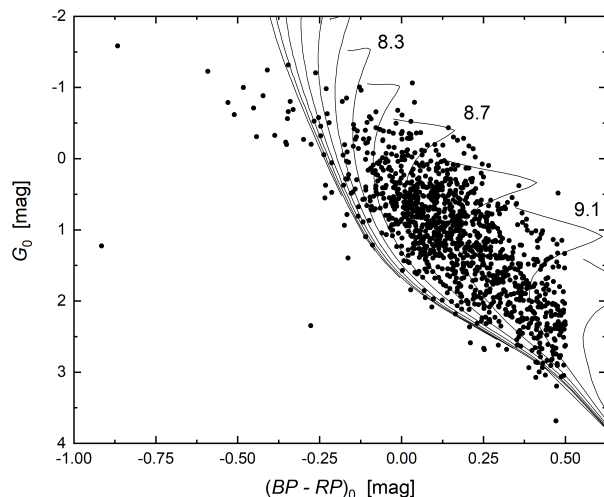


Fig. 4. G_0 versus $(BP - RP)_0$ diagram for the target star sample together with isochrones from Bressan et al. (2012) for solar metallicity $[Z] = 0.017$ dex. The values refer to the logarithmic ages of the isochrones. There is an obvious lack of stars close to the ZAMS.

about 1 Gyr. This supports the conclusions from the field star sample, which are described in the following section.

5. Discussion

This section summarises the results from our analysis, discussing different astrophysical aspects. Histograms illustrating the distributions of the distance from the Sun, mass, fraction of life spent on the main sequence, fraction of radius between ZAMS and TAMS, equatorial velocity, and ratio of equatorial to critical velocity are provided in Figure 3.

CMD: Figure 4 presents the G_0 versus $(BP - RP)_0$ diagram for the target star sample together with isochrones from Bressan et al. (2012) for solar metallicity $Z = 0.017$ dex. We find 35 objects (3%) not covered by the isochrone grid, in accordance with the results from other studies (Hümmerich et al. 2020). The reasons are unknown. The preference away from the ZAMS is apparent visually and cannot be explained with the chosen metallicity (Faltová et al. 2021).

Distance: Most of our sample stars are situated between 1000 and 6000 pc from the Sun. They are populating the first three quadrants in the Galactic disk, where the reddening cannot be neglected. All stars are members of the thin or thick disk (Vieira et al. 2022).

Mass: We see a peak of the mass distribution at about two solar masses, which corresponds to a spectral type of about A2. Otherwise, the spectral range from F1 to B8 is well populated with an apparent lack of more massive stars. The reason is unclear: there was no selection effect on astrophysical parameters.

$\tau(\text{age})$ and $\tau(\text{radius})$: It is clear that mCP stars are already present when they reach the ZAMS, as reported before in studies that investigated members of young open clusters (Pöhl et al. 2005). Subsequently, a constant increase in the number of stars up to a peak at about 65% of the main-sequence lifetime is reached. The diffusion timescale is much shorter and therefore not adequate to account for these observations (Michaud et al. 1981). One explanation might be an active dynamo that is driving and enhancing the magnetic field. However, for such a dynamo to work, differential rotation is needed (Kitchatinov & Olemskoy 2011), which is only observed for a small frac-

tion of upper main-sequence (Reiners & Royer 2004) and mCP (Mikulášek et al. 2018) stars. It was stated by Ammler-von Eiff & Reiners (2012) that no differential rotators are known with effective temperatures higher than 7400 K, a fact that has not been challenged since.

The distribution of the relative radii of our sample stars is quite different. For a constant mass, the radius increases from ZAMS to TAMS by a factor of about 2.4. Assuming that the total magnetic flux is conserved, it is distributed over a larger surface at the TAMS and thus becomes locally weaker. This influences the diffusion rates and the overall element abundances on the surface. The $\tau(\text{radius})$ distribution is symmetric with a peak at 45% of the TAMS value and therefore different than the distribution of ages. Together, these two distributions define the astrophysical parameter space where mCP stars are most commonly found. This is essential information not only for models but also for a further search for new class members.

Rotational velocity: Models predict that surface abundance patterns created by the diffusion of elements are destroyed by mixing induced by meridional circulation as a consequence of rotation (Turcotte 2003). However, the actual critical rotational velocity depends on the stellar mass and the strength of the magnetic field (Shore & Adelman 1976). The guide value is about 125 km s^{-1} . This amounts to about 40% of the critical velocity. In total, we identified 38 stars exceeding a v_{equ} of 150 km s^{-1} , with extreme values up to 260 km s^{-1} . The estimated statistical error is about 5 km s^{-1} .

We double-checked the 38 fast rotators to probe for any light curve or other peculiarities that may hint that these stars are not ACV variables and hence classical mCP stars. However, none were found: all stars show light variability in accordance with rotational modulation and pass the strict criteria imposed in the selection process (cf. Section 3.1).

A possible explanation is that we see the fast rotation of a cool companion star in an undetected spectroscopic binary system. It is well known that such short-period objects exist (Sowmya et al. 2022; Lu et al. 2022). However, such a possible companion would be between six to ten magnitudes fainter than the primary component. We can therefore rule out this scenario if we scale the observed amplitude to those surveyed in the listed references.

6. Conclusion

The available spectral data confirm that the employed selection process is highly efficient for detecting ACV variables and that the final sample of 1232 stars can be regarded as a pure sample of mCP stars.

In summary, we are confident that all 38 fast rotating stars are ACV variables. This interesting finding is in line with the results of Mikulášek et al. (2022), who identified an equatorial velocity of $v_{\text{equ}} = 230 \text{ km s}^{-1}$ for the well-established CP2 star HD 60431 and should now be aligned with the oblique rotator and diffusion models. Basic questions, such as how surface spots can manifest at such high rotational velocities, are still unanswered. Maybe a strong magnetic field stabilises the stellar atmosphere sufficiently. We therefore strongly encourage further detailed studies of these objects, in particular polarimetric measurements or the search for Zeeman splitting of lines, which will shed more light on the individual magnetic field characteristics. Due to the relative faintness of our target stars, however, such measurements can only be performed with the largest ground-based telescopes and a significant amount of observing time.

Acknowledgements. We want to thank the referee for carefully reading our manuscript and giving such constructive comments, which substantially helped improve the quality of the paper. M. Prišegen is supported by the European Regional Development Fund, project No. ITMS2014+: 313011W085. Based on observations obtained with the Samuel Oschin 48-inch Telescope at the Palomar Observatory as part of the Zwicky Transient Facility project, which is supported by the National Science Foundation under Grant No. AST-1440341 and a collaboration including Caltech, IPAC, the Weizmann Institute for Science, the Oskar Klein Center at Stockholm University, the University of Maryland, the University of Washington, Deutsches Elektronen-Synchrotron and Humboldt University, Los Alamos National Laboratories, the TANGO Consortium of Taiwan, the University of Wisconsin at Milwaukee, and Lawrence Berkeley National Laboratories. Operations are conducted by COO, IPAC, and UW. Guoshoujing Telescope (the Large Sky Area Multi-Object Fiber Spectroscopic Telescope LAMOST) is a National Major Scientific Project built by the Chinese Academy of Sciences. Funding for the project has been provided by the National Development and Reform Commission. LAMOST is operated and managed by the National Astronomical Observatories, Chinese Academy of Sciences. This work has made use of data from the European Space Agency (ESA) mission *Gaia* (<https://www.cosmos.esa.int/gaia>), processed by the *Gaia* Data Processing and Analysis Consortium (DPAC, <https://www.cosmos.esa.int/web/gaia/dpac/consortium>). Funding for the DPAC has been provided by national institutions, in particular the institutions participating in the *Gaia* Multilateral Agreement. This publication makes use of data products from the Two Micron All Sky Survey, which is a joint project of the University of Massachusetts and the Infrared Processing and Analysis Center/California Institute of Technology, funded by the National Aeronautics and Space Administration and the National Science Foundation.

References

- Ammler-von Eiff, M. & Reiners, A. 2012, *A&A*, 542, A116
 Andrae, R., Fouesneau, M., Creevey, O., et al. 2018, *A&A*, 616, A8
 Andriillat, Y. & Jaschek, C. 1998, *A&A*, 337, 512
 Arenou, F., Luri, X., Babusiaux, C., et al. 2018, *A&A*, 616, A17
 Bailer-Jones, C. A. L., Rybizki, J., Fouesneau, M., Demleitner, M., & Andrae, R. 2021, *AJ*, 161, 147
 Bellm, E. C., Kulkarni, S. R., Graham, M. J., et al. 2019a, *PASP*, 131, 018002
 Bellm, E. C., Kulkarni, S. R., Graham, M. J., et al. 2019b, *PASP*, 131, 018002
 Bressan, A., Marigo, P., Girardi, L., et al. 2012, *MNRAS*, 427, 127
 Carrasco, J. M., Weiler, M., Jordi, C., et al. 2021, *A&A*, 652, A86
 Chen, X., Wang, S., Deng, L., et al. 2020, *ApJS*, 249, 18
 Cui, X.-Q., Zhao, Y.-H., Chu, Y.-Q., et al. 2012, *Research in Astronomy and Astrophysics*, 12, 1197
 Eker, Z. & Bakış, V. 2023, *MNRAS*, 523, 2440
 Faltová, N., Kallouš, K., Prišegen, M., et al. 2021, *A&A*, 656, A125
 Fitzpatrick, E. L. & Massa, D. 2007, *ApJ*, 663, 320
 Gaia Collaboration, Brown, A. G. A., Vallenari, A., et al. 2021, *A&A*, 649, A1
 Georgy, C., Granada, A., Ekström, S., et al. 2014, *A&A*, 566, A21
 Ghazaryan, S., Alecian, G., & Hakobyan, A. A. 2018, *MNRAS*, 480, 2953
 Ghazaryan, S., Alecian, G., & Hakobyan, A. A. 2019, *MNRAS*, 487, 5922
 Graham, M. J., Kulkarni, S. R., Bellm, E. C., et al. 2019, *Publications of the Astronomical Society of the Pacific*, 131, 078001
 Gray, R. O. & Corbally, C. J. 2014, *AJ*, 147, 80
 Gray, R. O. & Corbally, Christopher, J. 2009, *Stellar Spectral Classification*
 Green, G. M., Schlafly, E., Zucker, C., Speagle, J. S., & Finkbeiner, D. 2019, *ApJ*, 887, 93
 Green, G. M., Schlafly, E. F., Finkbeiner, D., et al. 2018, *MNRAS*, 478, 651
 Hall, D. S. 1976, in *Astrophysics and Space Science Library*, Vol. 60, IAU Colloq. 29: Multiple Periodic Variable Stars, ed. W. S. Fitch, 287
 Hampel, F., Ronchetti, E., Rousseeuw, P., & Stahel, W. 2011, *Wiley Series in Probability and Statistics* (John Wiley & Sons, Inc.), 503–509
 Hümmerich, S., Paunzen, E., & Bernhard, K. 2020, *A&A*, 640, A40
 Hunt, E. L. & Reffert, S. 2023, arXiv e-prints, arXiv:2303.13424
 Jagelka, M., Mikulášek, Z., Hümmerich, S., & Paunzen, E. 2019, *A&A*, 622, A199
 Khan, S. A. & Shulyak, D. V. 2007, *A&A*, 469, 1083
 Kitchatinov, L. L. & Olemskoy, S. V. 2011, *MNRAS*, 411, 1059
 Kozhevnikova, A. V. & Alekseev, I. Y. 2015, *Astronomy Reports*, 59, 937
 Krtićka, J., Mikulášek, Z., Lüftinger, T., et al. 2012, *A&A*, 537, A14
 Kupka, F., Paunzen, E., & Maitzen, H. M. 2003, *MNRAS*, 341, 849
 Lenz, P. & Breger, M. 2005, *Communications in Asteroseismology*, 146, 53
 Lu, Y. L., Curtis, J. L., Angus, R., David, T. J., & Hattori, S. 2022, *AJ*, 164, 251
 Maitzen, H. M., Pressberger, R., & Paunzen, E. 1998, *A&AS*, 128, 573
 Maitzen, H. M. & Seggewiss, W. 1980a, *A&A*, 83, 328
 Maitzen, H. M. & Seggewiss, W. 1980b, *A&A*, 83, 328
 Malkov, O. Y., Sichevskij, S. G., & Kovaleva, D. A. 2010, *MNRAS*, 401, 695
 Masci, F. J., Laher, R. R., Rusholme, B., et al. 2019, *PASP*, 131, 018003

- Maury, A. C. & Pickering, E. C. 1897, *Annals of Harvard College Observatory*, 28, 1
- Michaud, G., Megessier, C., & Charland, Y. 1981, *A&A*, 103, 244
- Mikulášek, Z., Krtička, J., Paunzen, E., et al. 2018, *Contributions of the Astronomical Observatory Skalnaté Pleso*, 48, 203
- Mikulášek, Z., Semenko, E., Paunzen, E., et al. 2022, *A&A*, 668, A159
- Montegriffo, P., De Angeli, F., Andrae, R., et al. 2023, *A&A*, 674, A3
- Netopil, M., Paunzen, E., Hümmerich, S., & Bernhard, K. 2017, *MNRAS*, 468, 2745
- Paunzen, E., Hümmerich, S., & Bernhard, K. 2021, *A&A*, 645, A34
- Paunzen, E. & Prišegen, M. 2022, *A&A*, 667, L10
- Paunzen, E., Stütz, C., & Maitzen, H. M. 2005, *A&A*, 441, 631
- Paunzen, E. & Vanmunster, T. 2016, *Astronomische Nachrichten*, 337, 239
- Pöhl, H., Paunzen, E., & Maitzen, H. M. 2005, *A&A*, 441, 1111
- Preston, G. W. 1971, *PASP*, 83, 571
- Preston, G. W. 1974, *ARA&A*, 12, 257
- Ratzenböck, S., Großschedl, J. E., Alves, J., et al. 2023, *arXiv e-prints*, arXiv:2302.07853
- Reiners, A. & Royer, F. 2004, *A&A*, 415, 325
- Saffé, C., Levato, H., & López-García, Z. 2005, *Rev. Mexicana Astron. Astrofis.*, 41, 415
- Shi, F., Zhang, H., Fu, J., Kurtz, D., & Xiang, M. 2023, *ApJ*, 943, 147
- Shore, S. N. & Adelman, S. J. 1976, *ApJ*, 209, 816
- Sowmya, K., Nèmec, N. E., Shapiro, A. I., et al. 2022, *ApJ*, 934, 146
- Stibbs, D. W. N. 1950, *Monthly Notices of the Royal Astronomical Society*, 110, 395
- Stigler, C., Maitzen, H. M., Paunzen, E., & Netopil, M. 2014, *A&A*, 562, A65
- Supikova, J. & Paunzen, E. 2021, in *OBA Stars: Variability and Magnetic Fields*, 1
- Turcotte, S. 2003, in *Astronomical Society of the Pacific Conference Series*, Vol. 305, *Magnetic Fields in O, B and A Stars: Origin and Connection to Pulsation, Rotation and Mass Loss*, ed. L. A. Balona, H. F. Henrichs, & R. Medupe, 199
- Vieira, K., Carraro, G., Korchagin, V., et al. 2022, *ApJ*, 932, 28
- Watson, C. L., Henden, A. A., & Price, A. 2006, *Society for Astronomical Sciences Annual Symposium*, 25, 47
- Zhao, G., Zhao, Y.-H., Chu, Y.-Q., Jing, Y.-P., & Deng, L.-C. 2012, *Research in Astronomy and Astrophysics*, 12, 723

Appendix A: Essential data and light curves for our sample stars

Table A.1, available in full at the CDS, lists the essential data for our sample stars.

Table A.1. Essential data for our sample stars, sorted by increasing right ascension (extract). The full table is available at the CDS. The columns denote: (1) ZTF ID; (2) ID; (3) Right ascension (J2000; *Gaia* EDR3); (4) Declination (J2000; *aia* EDR3); (5) Period from Chen et al. (2020); (6) *G* magnitude (*Gaia* DR2); (7) *G* magnitude error (*Gaia* DR2); (8) (*BP* – *RP*) colour (*Gaia* DR2); (9) (*BP* – *RP*) colour error; (10) (*g*1 – *y*) colour; (11) *a* index; (12) *E*(*B* – *V*); (13) Parallax (*Gaia* DR3); (14) Parallax error; (15) Mass; (16) Fractional age on the main sequence; (17) Fractional radius on the main sequence; (18) Equatorial velocity; (19) Ratio of the equatorial and breakup velocity; (20) Spectral type.

(1)	(2)	(3)	(4)	(5)	(6)	(7)	(8)	(9)	(10)	(11)	(12)	(13)	(14)	(15)	(16)	(17)	(18)	(19)	(20)
ZTF0000041.86+631059.3	430083701322198016	10174456	63.183145	2.022767	13.3856	0.0009	0.4354	0.0041	9.741	1.737	0.341	0.3222	0.0117	2.53	0.76	0.53	78.3	0.24	
ZTF0000049.14+580009.1	422632585891909632	0.204771	58.002501	4.233268	13.0044	0.0012	0.7462	0.0050	11.719	3.243	0.408	0.5623	0.0157	2.12	0.79	0.62	36.6	0.12	
ZTF0000049.29+560741.1	420909067055294976	0.205423	56.128087	3.187368	14.6264	0.0011	0.6924	0.0058	10.439	1.664	0.200	0.3366	0.0219	1.67	0.69	0.42	35.6	0.12	
ZTF0000049.80+630653.9	430082911048271360	0.282551	63.114962	1.451780	13.2359	0.0008	0.5658	0.0042	10.676	2.041	0.410	0.3155	0.0105	2.65	0.88	0.80	136.0	0.46	
ZTF0000109.59+632305.7	431593630022392000	0.289977	63.384089	4.230083	13.8605	0.0008	0.6201	0.0039	10.337	2.706	0.415	0.2883	0.0129	2.38	0.80	0.65	39.7	0.13	
ZTF0000310.20+631736.2	4315936975551028736	0.792539	63.293393	3.651281	13.7526	0.0010	1.1375	0.0056	10.337	2.706	0.415	0.2883	0.0129	2.38	0.80	0.65	39.7	0.13	
ZTF0000318.72+592646.6	42326999339745408	0.828042	59.446267	1.889031	14.9951	0.0015	0.9864	0.0062	9.614	3.280	0.540	0.3543	0.0215	1.83	0.64	0.38	61.5	0.19	
ZTF0000320.10+595719.9	432313355390307200	0.671295	59.955527	2.194480	13.1024	0.0010	0.3591	0.0050	11.126	3.154	0.633	0.3212	0.0112						
ZTF0000340.89+644505.5	423139513181384192	0.920394	64.571531	8.445031	14.0842	0.0012	1.0062	0.0062	13.005	4.796	0.703	0.2875	0.0168	2.58	0.93	0.97	25.6	0.09	
ZTF0000340.91+623146.9	430027179553703552	0.920462	62.529681	2.005254	14.7932	0.0031	0.8354	0.0138			0.563	0.2510	0.0198	2.22	0.74	0.53	73.4	0.24	
ZTF0000400.12+642128.1	431749564514884352	1.000544	64.357803	2.433503	16.6064	0.0013	1.2179	0.0085			0.656	0.1907	0.0435	1.72	0.64	0.36	45.6	0.14	
ZTF0000400.34+634528.6	4316170399007033472	1.001421	63.757946	1.722651	16.3320	0.0019	0.8074	0.0098			0.487	0.2220	0.0375	1.76	0.19	0.05	47.1	0.13	
ZTF0000430.91+633115.1	431607212121962112	1.128801	63.520859	2.814172	16.3703	0.0019	1.0169	0.0087			0.471	0.1778	0.0417	1.69	0.67	0.39	39.7	0.13	
ZTF0000453.11+643446.7	431759391399934464	1.221324	64.579654	4.599917	15.7751	0.0006	1.1203	0.0041	10.804	2.301	0.538	0.4689	0.0587	1.49	0.13	0.02	16.1	0.04	
ZTF0000500.54+640951.9	431723794710271488	1.252267	64.164416	4.946422	14.2421	0.0012	0.8109	0.0055	13.323	3.444	0.775	0.1991	0.0152	3.82	0.76	0.48	38.0	0.11	
ZTF0000520.70+604135.4	429317960188135296	1.336265	62.752815	3.671449	15.1011	0.0009	0.7980	0.0043			0.644	0.2391	0.0212	2.42	0.59	0.31	34.7	0.10	
ZTF0000526.28+583002.9	423076440687524992	1.359555	58.500809	2.186827	15.5857	0.0013	0.9696	0.0056	12.774	3.770	0.605	0.1530	0.0288	2.24	0.83	0.71	77.9	0.27	
ZTF0000527.78+625005.0	430014225928748928	1.365792	62.834728	4.349762	14.3635	0.0007	0.6456	0.0038			0.558	0.2277	0.0163	2.78	0.73	0.47	36.4	0.11	
ZTF0000551.03+624510.1	430012645380856960	1.462665	60.693161	5.213785	12.6493	0.0008	0.6882	0.0052			0.319	0.9322	0.0109	1.79	0.57	0.29	20.3	0.06	
ZTF0000618.06+623707.3	430007319621536256	1.575269	62.618700	3.289776	15.9185	0.0009	1.0531	0.0051			0.628	0.2158	0.0301	1.90	0.64	0.38	36.2	0.10	
ZTF0000635.95+594051.6	423247453410415744	1.649819	59.680993	1.659816	15.2871	0.0010	0.8731	0.0064			0.535	0.2778	0.0248	1.91	0.57	0.29	66.2	0.20	
ZTF0000713.79+634446.5	431660465409284992	1.807494	63.746253	1.362058	15.2988	0.0008	0.5878	0.0043	10.126	3.132	1.610	0.4019	0.0378	2.23	0.85	0.79	34.7	0.12	
ZTF0000714.47+630842.6	528526997434410880	1.810308	67.145144	5.152370	16.2636	0.0019	2.3053	0.0115	14.459	4.126	0.495	0.2336	0.0223	2.33	0.66	0.39	28.0	0.08	
ZTF0000728.72+604238.5	429397571702143616	1.869691	60.710681	4.813121	14.7596	0.0005	0.6558	0.0030	8.054	5.848	0.366	0.5060	0.0189	1.55	0.46	0.17	13.0	0.04	
ZTF0000745.46+603122.5	429300608520427008	1.939435	60.522902	6.683301	14.7356	0.0003	0.8876	0.0034	10.945	3.756	0.920	0.5995	0.0109	2.22	0.98	1.05	71.9	0.28	
ZTF0000858.22+694045.7	530739146110430080	2.242614	69.679361	2.926237	13.4953	0.0012	1.4276	0.0023	10.654	3.617	0.625	0.4280	0.0216	2.28	0.76	0.55	37.3	0.12	
ZTF0001019.45+644548.8	432102267224418176	2.581093	63.457570	4.087818	13.8197	0.0014	0.8993	0.0063			0.507	0.4086	0.0206	1.79	0.71	0.46	17.7	0.06	
ZTF0001038.63+594220.8	429059025197785728	2.660965	59.705776	6.943025	14.6724	0.0006	1.0211	0.0063	9.984	2.249	0.898	0.1976	0.0280	2.60	0.75	0.53	58.6	0.18	
ZTF0001056.46+642626.5	431887072184295424	2.735301	64.440717	2.739042	15.5147	0.0010	1.1315	0.0051			0.273	0.6490	0.0134	2.09	0.47	0.21	138.6	0.39	
ZTF0001112.69+574452.5	42247257590872960	2.802903	57.747908	0.765706	12.7760	0.0006	0.4041	0.0035	10.950	2.967	0.884	0.1669	0.0326	2.61	0.56	0.28	9.9	0.03	
ZTF0001153.24+643005.5	431907275711549824	2.971880	64.501523	12.892051	15.9590	0.0014	1.0598	0.0061	12.271	4.238	0.356	0.3780	0.0130	2.30	0.59	0.32	68.8	0.20	
ZTF0001204.14+623936.6	431310378339767168	3.017297	62.660170	1.808221	13.6627	0.0007	0.4666	0.0033	10.269	2.117	0.517	0.3211	0.0157	2.20	0.84	0.75	24.7	0.09	
ZTF0001218.47+603439.1	429218729264606592	3.076986	60.577530	6.958805	14.1988	0.0007	0.9023	0.0051			0.428	0.3060	0.0122	2.90	0.83	0.65	76.7	0.24	
ZTF0001322.71+633434.6	431470632159430144	3.344665	63.576282	2.437494	13.1437	0.0008	0.4907	0.0050			0.629	0.2463	0.0367	1.81	0.46	0.19	63.3	0.18	
ZTF0001339.71+602722.9	429167288428957568	3.415491	60.456360	1.533054	16.1140	0.0020	1.0177	0.0133			0.609	0.2483	0.0140						
ZTF0001445.88+623546.0	431254028366483968	3.691193	62.596110	1.909181	13.7831	0.0007	0.5602	0.0051			0.696	0.2483	0.0140	1.74	0.58	0.29	45.6	0.14	
ZTF0001446.92+625710.7	431287769630500480	3.695520	62.952972	2.299285	16.3118	0.0024	1.0965	0.0112	12.634	4.664	0.514	0.2960	0.0234	1.90	0.48	0.21	79.6	0.23	
ZTF0001450.13+631219.8	431433145683973888	3.708931	63.205505	1.270681	15.2653	0.0010	0.8220	0.0060			0.763	0.1597	0.0399	1.92	0.89	0.88	55.3	0.21	
ZTF0001457.48+623501.0	431253856567801088	3.739507	62.583618	3.127105	16.3299	0.0010	1.4402	0.0069	14.053	4.649	0.634	0.2123	0.0162	2.47	0.99	1.10	15.0	0.06	
ZTF0001519.54+634008.1	431428300959455744	3.831463	63.668919	15.320009	14.4333	0.0010	0.9377	0.0049	10.235	2.756	0.621	0.2058	0.0257	2.07	0.80	0.65	49.6	0.17	
ZTF0001542.54+624753.9	431279832531026048	3.927311	62.798316	3.139875	15.5410	0.0010	1.0720	0.0058	10.179	2.493	0.687	0.3476	0.0188	2.16	0.67	0.42	74.2	0.23	
ZTF0001545.14+643417.7	431946789406738432	3.938129	64.571592	1.782231	14.7195	0.0008	0.9810	0.0038	10.376	2.402	0.515	0.3218	0.0193	1.96	0.70	0.48	25.1	0.08	
ZTF0001601.82+605057.1	429545627813160192	4.007604	60.849202	5.273914	14.8017	0.0010	0.9200	0.0060	10.991	2.569	0.499	0.2812	0.0191	2.01	0.75	0.54	85.9	0.28	
ZTF0001619.48+584544.4	422955292553097472	4.081181	58.762330	1.636320	14.8918	0.0006	0.8969	0.0034			0.490	0.2376	0.0155	2.69	0.86	0.75	65.3	0.22	
ZTF0001639.31+632910.3	431417134044654080	4.163834	63.486206	2.958571	13.9559	0.0010	0.6424	0.0048	11.992	4.385	0.391	0.4080	0.0124	2.15	0.63	0.38	41.0	0.12	
ZTF0001648.83+624310.2	43128131000032128	4.203495	62.719501	3.106824	13.7082	0.0009	0.5887	0.0043	10.715	2.674	0.685	0.2655	0.0301	1.91	0.66	0.40	55.3	0.17	
ZTF0001717.85+614459.2	429711997667191936	4.324396	61.749780	2.191678	15.7613	0.0012	1.1243	0.0064	10.751	2.674	0.433	0.3467	0.0202	1.73	0.62	0.34	58.5	0.18	
ZTF0001742.73+583243.8	422200237304252800	4.428095	58.545489	1.864920	15.0093	0.0008	0.9108	0.0052	11.420	2.543	0.529	0.4321	0.0160	2.05	0.52	0.25	84.7	0.24	
ZTF0001751.41+593607.4	428263700334022528	4.464262	59.602048	1.289917	14.2339	0.0008	0.7667	0.0029			0.6760	0.0029	0.0160	2.46	0.81	0.64	70.4	0.23	
ZTF0001843.03+725256.6	537329412648335616	4.679357	72.882386	2.414676	13.1813	0.0015	0.4760	0.0075			0.330	0.3535	0.0106	2.46	0.81	0.64	70.4	0.23	